# A Virtual Source Method for the prediction of the sound field around rigid obstacles

**Penelope Menounou[1], Spyros Bougiesis[1], Yannis Kallinderis[1], Panos Antonellis[1]**

[1]Department of Mechanical Engineering and Aeronautics, University of Patras, Patras, Greece
(email: menounou@upatras.gr)

**Abstract**

The prediction of the acoustic field produced by a known sound source around a rigid 2-D obstacle is investigated. Consider, for example, the cross section of a house (simplified as a polygon) or an ancient theater (simplified as right-angled steps). Sound is reflected from the edges of the cross section and diffracted by its vertices. A method is presented that (i) identifies all propagation paths between source and receiver, (ii) associates each propagation path with a corresponding virtual source and (iii) employs newly presented empirical formulas to compute the contribution of each virtual source at the receiver location. The employment of empirical formulas instead of analytical solutions for the virtual sources reduces the computational time by orders of magnitude. Results agree favorably with available measured data. As opposed to traditional computational aeroacoustics methods, the computational cost does not depend on the frequency or the propagation distance. Finally, as opposed to other similar methods (that handle the propagation effects separately), the proposed method accounts for high order diffractions. Also, it can work directly in the time domain for the prediction of the impulse response

**Keywords:** virtual sources, higher-order diffraction, empirical formulas, impulse response

## 1 Introduction

The acoustic field that a known sound source produces around a rigid 2-D obstacle is investigated**.** The problem is usually handled with computational aeroacouctics methods (e.g. [1]). In this category belong the acoustic analogies methods, the Kirchhoff method or other boundary element methods, computational fluid dynamics methods, or the two step computational fluid dynamics/computational aeroacoustics formulations. These methods have been used extensively and allow predictions around complex geometries and through complex propagation environments. Their main disadvantage is the computational cost, which increases dramatically with increased propagation distances and increased source frequencies. A widely used alternative are virtual source methods, ray tracing and beam tracing methods, which have also been used extensively (e.g. [2]). A disadvantage of the ray tracing methods is the undersampling, (i.e the amount of rays emanating is not enough to sufficiently cover the whole space and thus find all propagation paths) or the creation of caustics. The present work is an extension to the virtual sources method. The virtual source method is based on creating virtual sources by mirroring the position of a physical or a virtual source. In the present work the effect of first order, as well as higher order diffraction is included. Every physically possible propagation path is identified and an elementary solution is associated to each identified propagation path (section 2).The method presented here can work directly both in the frequency and in the time domain (section 3). Existing analytical solutions termed *Directive Line Source Model (DLSM)* are employed for the formulation of the elementary solutions in both the frequency [3] and time domain [4]. The

time domain formulation allows the direct prediction of the impulse response and the involved computations are easy and fast to compute. The frequency domain formulations are time consuming, as they require the evaluation of Fresnel integrals. Employment of empirical formulas [5] (instead of the frequency domain elementary solution) reduces the computational time by orders of magnitude. Results are presented and compared with measured data in the frequency domain (section 4) and in the time domain (section 5). Virtual source methods do not suffer from undersampling or caustics nor is their computational cost increased with frequency or propagation distance. Finally, the presented method handles each propagation path separately and thus helps in the physical understanding of the studied problem (see section 5). Compared to our previously published work [6] on virtual source methods, the present work incorporates higher-order diffraction, the employment of empirical formulas and the direct formulation in the time domain.

## 2 Path identification and virtual source types

A ray tracing algorithm is employed to identify all propagation paths from source (S) to receiver ($R_{rec}$). The propagation path can be either (i) a direct path - a propagation path directly between source and receiver, if the receiver is directly illuminated by the source, or (ii) a path undergoing reflections on the edges $E_m$ and/or diffractions on the vertices $V_n$ of a 2-D geometry before reaching the receiver. The path $S$-$E_1$-$E_2$-$V_4$-$V_7$-$V_{10}$-$E_{11}$-$E_{12}$-$R_{rec}$ shown in Fig.1 is an example of a propagation path in the form of $S{\rightarrow}REF^{(M_1)}{\rightarrow}DIF^{(N)}{\rightarrow}REF^{(M_2)}{\rightarrow}R_{rec}$. $REF^{(M_1)}$ and $REF^{(M_2)}$ indicate reflection-only portions in the propagation path, where sound undergoes $M_1=2$ and $M_2=2$ successive reflections on the edges of the geometry and $DIF^{(N)}$ indicates a diffraction-only portion, where sound undergoes $N=3$ successive diffractions on the vertices of the geometry. The corresponding virtual source for a reflection-only portion is a *Virtual Point Source (VPS)*, while for a diffraction-only portion a *Virtual Edge Source* (*VES*). For the mixed path, such as $S{\rightarrow}REF^{(M1)}{\rightarrow}DIF^{(N)}{\rightarrow}REF^{(M2)}{\rightarrow}R_{rec}$, the virtual source is of a *Virtual Source of Mixed Type* (*VpeS*). The mixed type VpeS is essentially a VES corresponding to $DIF^{(N)}$ with its source being not the physical source S, but a virtual point source of $M_1$ order, and the receiver not the physical receiver, but a virtual receiver of $M_2$ order. For the path depicted in Fig.1 ($S$-$E_1$-$E_2$-$V_4$-$V_7$-$V_{10}$-$E_{11}$-$E_{12}$-$R_{rec}$), the virtual point source of $M_1=2$ order is created by 2 successive mirrorings of the physical source. The source illuminates the edge $E_1$, a virtual point source ($VPS^{(1)}$) is created that is located at the mirror location of the source with respect to edge $E_1$. The created point source $VPS^{(1)}$ illuminates the edge $E_2$, and a new virtual source ($VPS^{(2)}$) is created at the mirror location of $VPS^{(1)}$ with respect to the illuminated edge $E_2$. Associated with the mirroring is the distance that sound travels from the source to reach the first vertex $V_4$ of the propagation path after it has undergone $M_1=2$ successive reflections. Or equivalently, the distance between the last virtual point source $VPS^{(M_1=2)}$ and vertex $V_4$. Similarly, the virtual receiver of order $M_2=2$ is created by successive mirroring of the physical receiver 2 times, on the edges $E_{12}$ and $E_{11}$, until the last vertex $V_{10}$ of the propagation path is reached. This is the same path from the vertex $V_{10}$ to the physical receiver, but traveled on the opposite direction. Here, again, the associated distance is the total distance sound travels from vertex $V_{10}$ to reach the physical receiver.
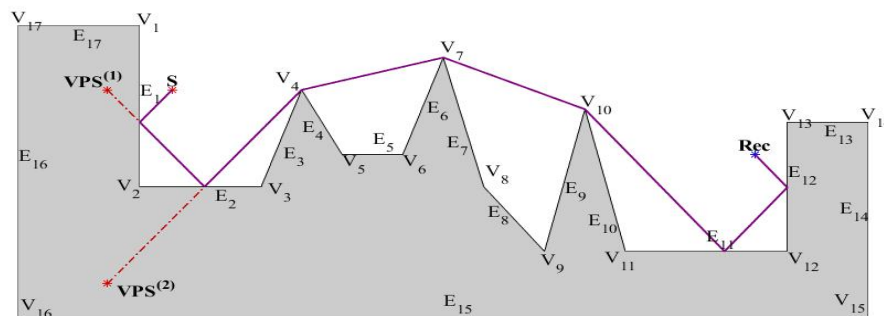


Figure 1 - Example of propagation path.

# 3    Computation of acoustics pressure

In the present section the mathematical expressions are provided for the different contributions in both the frequency and the time domain. In the present work four different types of contributions are considered: (i) the contribution from the incident field, (ii) the contribution from reflection-only paths, (iii) the contributions from diffraction-only paths, and (iv) contributions from mixed paths.

## 3.1    Frequency domain analytical solution

Contributions from the incident field are taken into account only if the receiver is directly illuminated by the physical source

$$P_{direct} = P_0 \frac{e^{ikr_{direct}}}{r_{direct}}, \tag{1}$$

where $r_{direct}$ is the distance between source and receiver and $P_0$ is the amplitude of the sound source. Contributions from reflections-only propagation paths (i.e. Virtual Point Sources) are evaluated as

$$P_{VPS}^{(M)} = P_0 \frac{e^{ik\bar{r}_{rp}^{(M)}}}{\bar{r}_{rp}^{(M)}}, \tag{2}$$

where $\bar{r}_{rp}^{(M)}$ is the distance between the M-th order VPS, (VPS$^{(M)}$) and the receiver. An existing analytical solution (DLSM) for diffraction in the frequency domain ([3][5]) is employed for the contributions from diffraction-only propagation paths (i.e. Virtual Edge Sources)

$$P_{VES}^{(N)} = \left( -\frac{i}{4} \frac{1}{r_o r_1} H_0^{(1)}\left(kL^{(1)}\right) D^{(1)} \right)\left( -\frac{i}{4} H_0^{(1)}\left(kr_2\right) D^{(2)} \right)\ldots\left( -\frac{i}{4} H_0^{(1)}\left(kr_N\right) D^{(N)} \right)\left(\frac{1}{2}\right)^{\bar{N}}, \tag{3}$$

where $H_0^{(1)}$ is the Hankel function of the first kind and of zero order, $L^{(1)}$ the distance $L^{(1)} = \sqrt{(r_0 + r_1)^2}$ (see Fig.2), $D^{(n)}$ a directivity function that corresponds to vertex $V_n$ and is associated to the wedge diffraction problem with wedge angle $\Omega_n$ (see Fig.2), and $\bar{N} < N$ is the number of vertices, if any, that share a common edge (in Fig.1 $V_4$ and $V_5$ share a common edge, while $V_4$ and $V_7$ do not). The directivity functions of each wedge problem, $D^{(n)}$, depend on the corresponding wedge angle $\Omega_n$ and on the radial and angular locations $r_n, \phi_n, r_{n-1}, \phi_o^{(n)}$ (see Fig.2)

$$D^{(n)}\left(r_{n-1}, r_n, \phi_0^{(n)}, \phi_n, \Omega_n, k\right) = D_1^{(n)}\left(r_{n-1}, r_n, \phi_0^{(n)}, \phi_n, \Omega_n, k\right) + D_2^{(n)}\left(r_{n-1}, r_n, \phi_0^{(n)}, \phi_n, \Omega_n, k\right) \tag{4}$$

$$D_{1,2}^{(n)} = sign(\Phi_{1,2}^{(n)}) 2\sqrt{2} u_{1,2}^{(n)} e^{-i\frac{\pi}{2}\left(u_{1,2}^{(n)}\right)^2 \left(\Phi_{1,2}^{(n)}\right)^2} \left( \overline{F(\infty)} + iF\left(u_{1,2}^{(n)} \left|\Phi_{1,2}^{(n)}\right|\right) \right) \tag{5}$$

where $F$ denotes the Fresnel integral, $\Phi_1^{(n)}, \Phi_2^{(n)}$ are functions of the angular locations $\phi_n, \phi_o^{(n)}$ and the wedge angle $\Omega_n$ and $u_1^{(2)}, u_2^{(2)}$ are functions of normalized distances

$$\Phi_1^{(n)} = \gamma_n \sqrt{2} \, \frac{\cos\left(\left(\varphi_n - \varphi_0^{(n)}\right)/\gamma_n\right) - \cos\left(\pi/\gamma_n\right)}{\pi \sin\left(\pi/\gamma_n\right)}$$

$$\Phi_2^{(n)} = -\gamma_n \sqrt{2} \, \frac{\cos\left(\left(2\pi - \varphi_n - \varphi_0^{(n)}\right)/\gamma_n\right) + \cos\left(\pi/\gamma_n\right)}{\pi \sin\left(\pi/\gamma_n\right)}, \quad \gamma_n = \left(2\pi - 2\Omega_n\right)/\pi \tag{6}$$

$$u_{1,2}^{(n)} = \sqrt{\frac{k r_n r_0 \pi}{L^{(n)} + R_{1,2}^{(n)}}}, \; R_1^{(n)} = \sqrt{r^2 + r_0^2 - 2 r r_0 \cos\left(\phi_n - \phi_0^{(n)}\right)}, \; R_2^{(n)} = \sqrt{r^2 + r_0^2 - 2 r r_0 \cos\left(\phi_n + \phi_o^{(n)}\right)} \tag{7}$$

Contributions from mixed paths are also computed via Eq.(3) but with the location of the source and the receiver being as indicated in section 2.
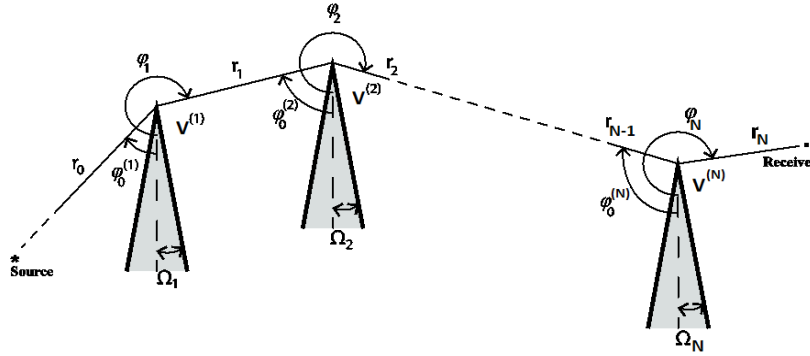


Figure 2 - Geometry of the problem of N successive diffractions.

## 3.2 Frequency domain empirical formulas

The computations for the direct path or the reflection-only paths are straight-forward and easy to perform. The diffraction contributions, on the other hand, are computationally expensive, as they require the evaluation of multiple Fresnel integrals. Empirical formulas are proposed instead. In the present work the empirical formulas presented in ref. [5] are employed. They provide the insertion loss $IL$

$$IL = -10 \log\left(\frac{P_d^{rms}(A)}{P_o^{rms}(A)}\right)^2, \tag{8}$$

where $P_d^{rms}(A)$ is the root mean square (rms) value of the diffracted field $P_d$ at A, and $P_o^{rms}(A)$ the rms value of the free field at the same location. The acoustic pressure can be obtained by the $IL$ as follows [5]:

$$P_{VES}^{(N)} = \frac{10 e^{-\frac{IL_{VES_{emp}}^{(N)}}{20}}}{R_{direct}} i e^{ikL_{tot} - i\pi/4}, \quad L_{tot} = \sum_{n=0}^{N} r_n, \tag{9}$$

where $R_{direct}$ is the Euclidian distance between source and receiver and the distances $r_n$ arre as shown in Fig.2. The empirical formulas for receivers in the shadow zone are:

$$IL_{VES_{emp}}^{(N)} = \sum_{n=1}^{N} IL_s^{(n)} + \sum_{n=1}^{N} IL_{sb1}^{(n)} + \sum_{n=1}^{N} \overline{IL}_{sp}^{(n)} + \overline{\overline{IL}}_{sp}^{(N)} + IL_w^{(1)} \tag{10}$$

$$IL_s^{(n)} = -20\log\left(10^{-IL_{s1}^{(n)}/20} + 10^{-IL_{s2}^{(n)}/20}\right)$$ (11)

$$IL_{s1}^{(n)} = 20\log\frac{\sqrt{2\pi N_1^{(n)}}}{\tanh\sqrt{2\pi N_1^{(n)}}} + 5, \qquad IL_{s2}^{(n)} = 20\log\frac{\sqrt{2\pi N_2^{(n)}}}{\tanh\sqrt{2\pi N_2^{(n)}}} + 5$$ (12)

$$N_1^{(n)} = \frac{(u_1^{(n)})^2\left|\Phi_1^{(n)}\right|^2}{2}, \quad N_2^{(n)} = \frac{(u_2^{(n)})^2\left|\Phi_2^{(n)}\right|^2}{2},$$ (13)

$$IL_{sb1}^{(n)} = 0.25*(1-\tanh\sqrt{10 N_1^{(n)}})(6\tanh\sqrt{N_2^{(n)}} - 2 - 20\log\left[1+\tanh\left(0.6\log\frac{N_2^{(n)}}{N_1^{(n)}}\right)\right]),$$ (14)

$$\overline{IL}_{sp}^{(n)} = -10\log\frac{1}{\left(L^{(1)}\right)^2 + L^{(1)}R_1^{(1)}}, \quad \text{for} \quad n=1 \quad \text{and} \quad -10\log\frac{1}{L^{(n)} + R_1^{(n)}} \quad \text{for} \quad n=2,...N$$ (15)

$$\overline{IL}_{sp}^{(N)} = -10\log\left(\left(\frac{1}{4}\right)^{\bar{N}}\bar{R}^2 r_1 r_2 .. r_{N-1}\right), \quad IL_w^{(1)} = -\left|(1+\gamma_1)\cot\left(\frac{\pi}{\gamma_1}\right)\right|\bigg/\left|\sqrt{u_2^{(1)}} + N_1^{(1)}\right|$$ (16)

### 3.3 Time domain analytical solutions

One of the advantages of the presented method is that it can work directly in the time domain providing the impulse response at a receiver location. The time domain counterparts of Eqs (1) and (2) of the direct signal and of the reflection-only signal are

$$p_{direct} = \delta\left(t - \frac{r_{direct}}{c}\right), \qquad p_{VPS}^{(M)} = \frac{1}{\overline{r}_{rp}^{(M)}}\delta\left(t - \frac{\overline{r}_{rp}^{(M)}}{c}\right),$$ (17)

where $\delta$ is the Dirac function. For the computation of the diffraction contribution, an existing time domain solution is employed [4]. Based on that solution, the time domain counterpart of the Eq. (3) is obtained :

$$p_{VES}^{(N)} = \left(-\frac{1}{4\pi}\frac{1}{rr_0}\frac{2}{\sqrt{t^2-(t_d^{(1)})^2}}\cdot H\left(t-t_d^{(1)}\right)d^{(1)}\right)*...\left(-\frac{1}{4\pi}\frac{1}{rr_0}\frac{2}{\sqrt{t^2-(t_d^{(n)})^2}}\cdot H\left(t-t_d^{(n)}\right)d^{(n)}\right)*..$$

$$...*\left(-\frac{1}{4\pi}\frac{1}{rr_0}\frac{2}{\sqrt{t^2-(t_d^{(N)})^2}}\cdot H\left(t-t_d^{(N)}\right)d^{(N)}\right)\left(\frac{1}{2}\right)^{\bar{N}}$$ (18)

where $H$ is the Heaviside function and $d^{(n)}$, similarly to the frequency domain, is the directivity function of the n-th wedge problem :

$$d^{(n)} = \overline{t_{d1}^{(n)}}\cdot\Phi_1^{(n)}\cdot\frac{\sqrt{t/t_d^{(n)}+1}}{t-t_d^{(n)}+0.5\pi\cdot\overline{t_{d1}^{(n)}}\cdot(\Phi_1^{(n)})^2} + \overline{t_{d2}^{(n)}}\cdot\Phi_2^{(n)}\cdot\frac{\sqrt{t/t_d^{(n)}+1}}{t-t_d^{(n)}+0.5\pi\cdot\overline{t_{d2}^{(n)}}\cdot(\Phi_2^{(n)})^2}$$ (19)

$$t_d^{(1)} = \frac{L^{(1)}}{c}, \text{ for } n=1 \text{ , } t_d^{(n)} = \frac{r_n}{c}, \text{ for } n=2,...N, \text{ } \overline{t_{d1}^{(n)}} = \frac{r_n\cdot r_{n-1}\cdot\pi}{c\cdot\left(L+R_1^{(n)}\right)}, \text{ } \overline{t_{d2}^{(n)}} = \frac{r_n\cdot r_{n-1}\cdot\pi}{c\cdot\left(L+R_2^{(n)}\right)}.$$ (20)

5

It is noted that the time domain computations are much faster than the frequency domain computations and therefore there is no need for empirical formulas.

## 4    Frequency domain applications

The case of a wide barrier of infinite height is considered as shown in Fig.3(left). For receiver locations on the source side of the obstacle (region A) three paths are identified: (i) the direct path S-$R_{rec}$, (ii) a reflection-only path   S-$E_2$-$R_{rec}$ and (iii) a diffraction-only path S-$V_2$-$R_{rec}$ ($1^{st}$ order diffraction). For receivers in region B an additional diffraction-only path is identified S-$V_2$-$V_3$-$R_{rec}$ ($2^{nd}$ order diffraction). For receivers in region C the reflection-only path S-$E_2$-$R_{rec}$ is not longer present. For receivers in region D both the direct path S-$R_{rec}$ and the reflection-only path S-$E_2$-$R_{rec}$ disappear. Only diffraction paths can be identified. Specifically, the diffraction-only  paths  S-$V_2$-$R_{rec}$  ($1^{st}$  order  diffraction)  and  S-$V_2$-$V_3$-$R_{rec}$  ($2^{nd}$  order  diffraction)  can  be identified. For receivers in region E only the $2^{nd}$ order diffraction path S-$V_2$-$V_3$-$R_{rec}$ can be identified.
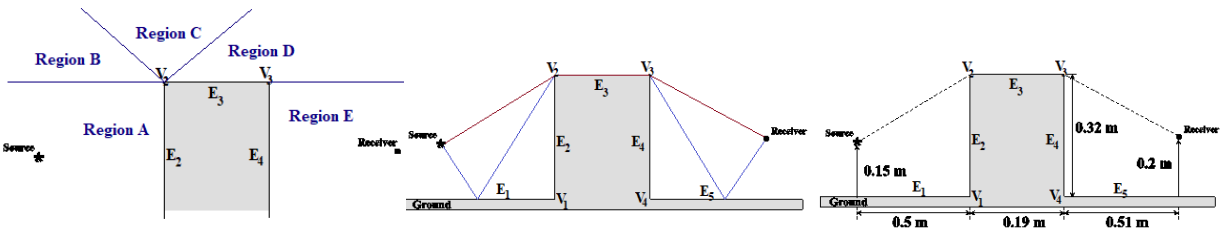


Figure 3 – Wide obstacle of infinite height and regions with different number of propagation paths around it (left), wide obstacle on rigid ground and paths for receivers behind the obstacle (middle), specific source-receiver configuration where measurements were taken (right) .

Figure 4 (right column) shows the sound field around the obstacle. If $2^{nd}$ order diffractions are ignored, region E is a complete shadow zone (see the middle column of the same figure). If both $1^{st}$ and $2^{nd}$ order diffractions are ignored, regions D and E become complete shadow zones (left column). The comparison shows that ignoring diffraction introduces errors, particularly in regions D and E. It should also be noted that the vertices $V_2$ and $V_3$ share a common edge and thus $\bar{N} = 1$ in Eq.(3).

The case of a wide barrier on a rigid ground is considered next [see Fig.3 (middle)]. The configuration gives rise to reflections from the barrier and also from the ground, as well as to diffraction by the vertices of the barrier. It is noted that only the vertices $V_2$ and $V_3$ of the barrier give rise to diffraction. The vertices $V_1$ and $V_4$ correspond to non-diffracting angles $2\Omega = 270^0$. Non-diffracting angles produce no diffraction field. As discussed previously, we focus our attention to receiver locations in the shadow zone behind the obstacle. Four different paths are identified in the shadow zone [see Fig.3 (middle)]. The first is a diffraction-only path S-$V_2$-$V_3$-$R_{rec}$, the other three are of the mixed type involving ground reflections on either side of the obstacle (S-$E_1$-$V_2$-$V_3$-$R_{rec}$, S-$V_2$-$V_3$- $E_5$-$R_{rec}$) and on both sides of the obstacle (S-$E_1$-$V_2$-$V_3$-$E_5$- $R_{rec}$).

Figure 5 shows results obtained by the analytical solution (DLMS) and by the empirical formulas for receiver locations in the shadow zone. It is shown that the results obtained by the analytical solutions are close to the results obtained by the empirical solutions. For the results depicted in Fig.5, the maximum difference between DLSM and empirical is less than 2.5 dB, while the discrepancies reduce with increasing frequency. The main advantage of the empirical formula is that it is order of magnitude faster to compute. For a receiver grid of 165000 receivers, the evaluation of the empirical formula takes 8 min to compute, while for the analytical solutions 20 hours. The comparisons have been performed with MATLAB on a personal computer with AMD Ryzen 7 3700X 4.0 GHz processor.
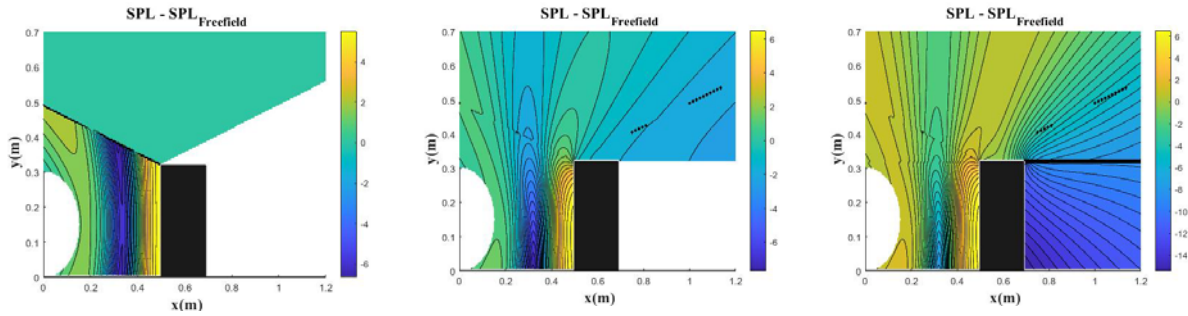
Figure 4 - Wide obstacle of infinite height: geometrical acoustics contributions only (left); geometrical acoustics contributions and 1st order diffraction contributions (middle); geometrical acoustics contributions and 1st and 2nd order diffraction contributions (right); $f = 500\,\text{Hz}$

Finally, results are compared with measured data. The calculations are done for a fixed source and receiver location [see Fig.3 (right)] at different frequencies with both the analytical solution and the empirical formula. Figure 5 shows that predictions obtained by the analytical solution and the empirical formulas are in good agreement with each other and also in reasonably good agreement with measured data taken from [7].
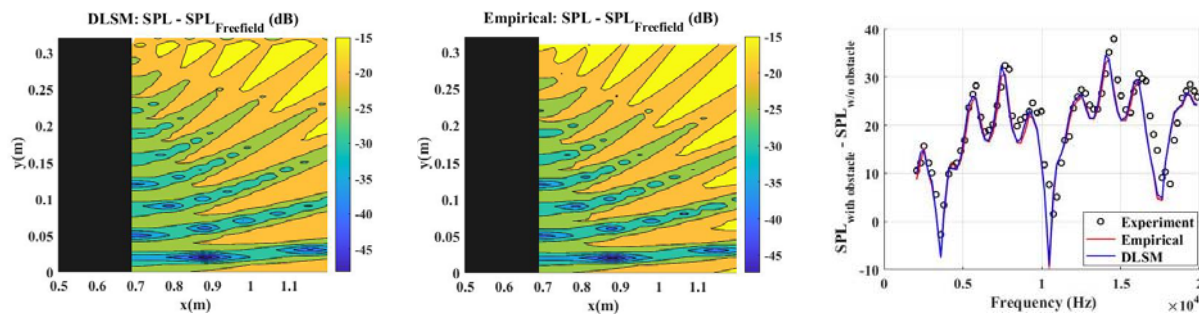


Figure 5- Wide obstacle on rigid ground : predicted sound field in the shadow zone employing analytical solutions (left) and empirical formulas (middle) for the diffraction contribution, $f = 5000\,\text{Hz}$; comparisons between predictions and measured data for the configuration in Figure 3 taken from [7](right).

## 5    Time domain applications

A cross section of the theater of Epidaurus is considered simplified as right-angled steps. The cross section shown in Fig.6 (left) shows the arrangement of the real theater (depicting the lower koilon, the upper koilon and the diazoma between them) but the geometrical details (curvatures and recesses) of each step are ignored. The sound source is located in the middle of the orchestra (12.86 m horizontal distance from the first step) at a height of 1.485 m. The source is a Dirac function and the impulse response is sought at a listener seating at an arbitrary row (at a height of 0.8 m above each seat and 0.2 m away from the front vertex of each seat).

Several paths are identified. Consider the geometrical acoustics contributions first. The following paths are identified: (i) the direct path (at all listeners) (ii) the reflection-only path S-orchestra-$R_{rec}$ (at all listener locations), (iii) the reflection-only path S-back of the seat- $R_{rec}$ (for listeners at the rows 1-4 and 9-24), (iv) the reflection-only path S-orchestra- back of seat- $R_{rec}$ (for listeners at rows 1-6). Figure 6 (right) shows the acoustics signals associated with the above paths at selected listener locations.

Paths associated with diffraction by the vertices of the steps are also identified. For example, direct sound from the source reaches the vertices of all steps and gives rise to diffracted signals that eventually reach a listener seating at an arbitrary row. Figure 7 shows the diffracted signals that are created by the vertices of all steps and reach a listener at the 20th step. It is noted that the depicted diffracted signals originate from the direct sound: the corresponding paths are S-vertex- $R_{rec}$ (for all vertices). Similar trails of diffracted signals originate from sound reflected on the orchestra. The corresponding paths are S-orchestra-vertex- $R_{rec}$, for all vertices. Similarly, with the other reflection-only paths mentioned above. The diffracted signals depicted in Fig.7regard 1st order diffraction. Second order diffraction has not been considered, since all listeners are illuminated directly by the source and higher order diffraction is not expected to affect the results (see discussion in previous section).
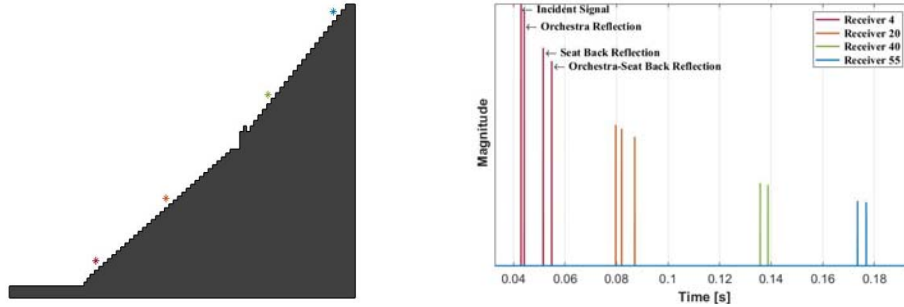


Figure 6-Cross section of the theater of Epidaurus (left), geometrical acoustics contributions at selected rows (right).

The study of the results has shown that, irrespective of the listener position, diffracted signals coming from vertices below the listener come close together and with relative small amplitude. On the other hand, diffracted signals from vertices above the listener come further apart, some with very large amplitude and almost all with negative polarity (see Fig.7)
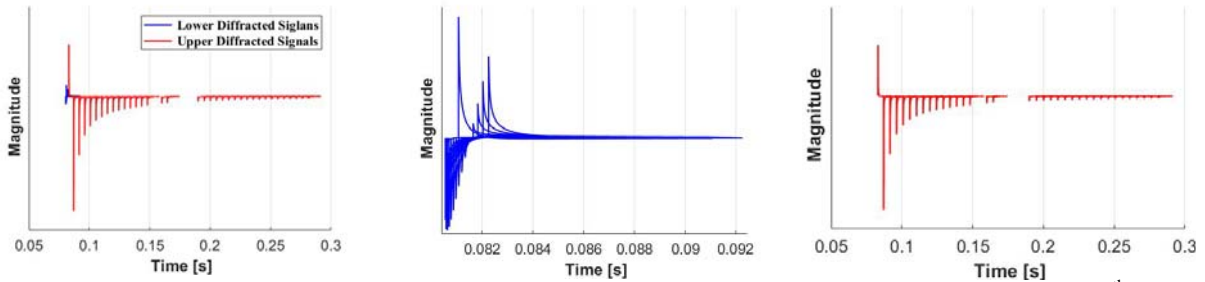


Figure 7 – Diffraction contributions originating from the direct signal from the sound source at the 20th row (left); diffraction contributions coming from vertices below (middle) and above (right) the receiver.

One of the advantages of the presented method is that it handles each propagation effect separately. Consider the total impulse response predicted at the 20th step as shown in Fig.8 (left). The Speech Echo Criterion is a acoustic parameter defined ([8],[9])

$$TS = \int_0^\infty t \cdot |g(t)|^{2/3}\, dt \left/ \int_0^\infty |g(t)|^{2/3}\, dt \right. , \qquad (21)$$

where $g(t)$ is the total impulse response at the receiver location. The lower the value of $TS$, the better the intelligibility at the receiver location. The Speech Echo Criterion $TS$ is computed at each step of the theater and is depicted in Fig.8 (right). The criterion is computed for the total impulse solutions (Geom+$D_{tot}$) but also for various different subset of contributions: only the geometrical acoustics contributions (Geometrical), the geometrical acoustics contributions together with all diffracted contributions coming from steps lower than the receiver (Geom+$D_{Low}$) and the geometrical acoustics contributions together with all diffracted contributions coming from steps higher than the receiver (Geom+$D_{up}$). The following observations can be

made. If only the geometrical acoustics contributions were present (i.e. the direct signal and the reflections from the orchestra or the back of the seats), the intelligibility would have been the best among the cases considered. The diffracted signals coming from lower seats do not affect the intelligibility. On the other hand, the diffracted signals coming from the upper seats considerably deteriorate the intelligibility. Also, the diffracted signals from the upper seats seem to be the most important contribution to the total field. Finally, the following observation is worth mentioning. The intelligibility is better at the seats closer to the orchestra (and thus to the sound source). Geometrical acoustics contributions and lower diffracted signals cause the intelligibility to vary substantially between the lower seats (first rows) and the upper seats (last rows). The upper diffracted signals smooth out the discrepancies in the intelligibility between the first seats/rows and the last seat/rows.
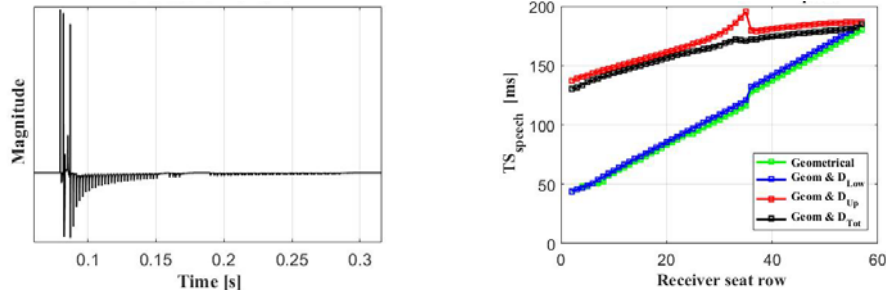


Figure 8 - Predicted total impulse response at the 20th row (left), predicted Speech Echo Criterion $TS$ on each row for different subset of acoustic contributions.

Finally, the predicted impulse responses are used to compute two acoustics indices. Firstly, the Clarity Index (or Klarheit), which characterizes the transparency of the sound ([8],[9]) is computed

$$C_{80} = 10\log\left( \int\limits_{0}^{80ms} \left\{ g\left(t\right)^{2}\right\} dt \middle/ \int\limits_{80ms}^{\infty} \left\{ g\left(t\right)^{2}\right\} dt \right) = 10\log\frac{E_{0-80}}{E_{80-\infty}} . \tag{22}$$

The Clarity Index compares the energy that arrives at the receiver the first 80 ms ( $E_{0-80}$ ) with the energy that arrives after the 80 ms ( $E_{80-\infty}$ ). The higher the value of the Clarity Index at a receiver location, the better the intelligibility of speech. The index $C_{80}$ is computed at all receiver/step locations and the results are shown in Fig.9 (left).
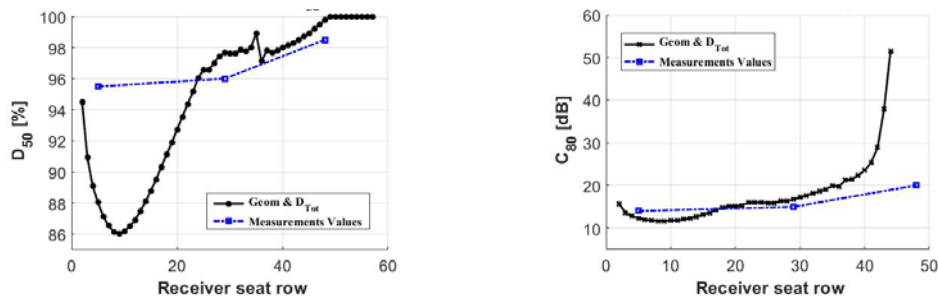


Figure 9 - Comparison of predicted values of Clarity Index $C_{80}$ (left) and Definition Index $D_{50}$ (right) with measured values taken at the theater of Epidaurus from ref. [10].

It is noted that the predicted values of $C_{80}$ are reasonably close to the measured valued at receivers at 5th step and the 29th step (1.65dB difference at the 5th step and 1.69 dB difference at the 29th step ). The measured data are taken from field measurements in the theater of Epidaurus published in ref [10]. The discrepancy between measured data and predictions at higher steps is expected, because the details of the geometry at the high end of the upper koilon are not included in the simplified geometry considered. Also, the geometrical

acoustics contributions that arrive from the sides of the curved koilon after 80 ms are not modeled by our simplified 2D model. The sharp increase in the values of $C_{80}$ for the upper seats predicted by our model is attributed to the latter simplification: no arrival after 80ms are predicted.

The Definition Index (or Deutlichkeit) is also computed ([8],[9])

$$D_{50} = \left( \int\limits_0^{50ms} \left\{ g\left(t\right)^2 \right\} dt \bigg/ \int\limits_0^{\infty} \left\{ g\left(t\right)^2 \right\} dt \right) \cdot 100\% = \frac{E_{0-50}}{E_{0-\infty}} \cdot 100\% \ . \tag{23}$$

The value of the Definition Index is directly related to the intelligibility of speech. The higher the value of the Definition Index the better the intelligibility. Comparisons with measured data taken from ref [10] show that at the 5th step the predicted value deviates from the measured value by 7 % , while at the 29th step and the 48th step the agreement is very good (the deviations are 0.67% and 1.28% respectively) .

## 6   Conclusions

A virtual source method has been presented that predicts the sound field around rigid 2D obstacles. The method works both in the frequency and time domain and results are in good agreement with available experimental data. Employment of empirical formulas in the frequency domain reduces the computational time by orders of magnitude.

## References

[1] Kurbatskii, KA.; Mankbadi, RR.; Review of Computational Aeroacoustics Algorithms. *International Journal of Computational Fluid Dynamics*, Vol. 18(6), 2008, pp. 533-546.

[2] Savioja, L.; Svensson, P.U.; Overview of geometrical room acoustic modeling techniques. *Journal of Acoustical Society of America*, Vol. 138, 2015, pp.708-730.

[3] Menounou, P.; Nikolaou, P. An Extension to the Directive Line Source Model for Diffraction by Half Planes and Wedges. *Acta Acustica United with Acustica*, Vol. 102, 2016, pp 307-321.

[4] Menounou, P.; Nikolaou, P. Analytical model for predicting edge diffraction in the time domain. *Acoustical Society of America*, Vol. 142 (6), 2017, pp 3580-3592.

[5] Menounou, P.; Asimakopoulos, V. Empirical formulas for predicting the insertion loss behind wedges. *Applied Acoustics*, Vol. 182, 2021, pp 108166.

[6] Menounou, P.; Klagkos, C.; A virtual source method for the prediction of the sound field around complex geometries. *23rd International Congress on Sound & Vibration*, Athens Greece, July 2016, In CD-ROM.

[7] Wadsworth, G.J.; Chambers, J.P. Scale experiments on the insertion loss of wide and double barriers. *Acoustical Society of America*, Vol. 107, 2000, pp 2344-2350.

[8] International Organization for Standardization. Acoustics-Measurement of Room acoustics parameters Part 1-Reverbation time in ordinary rooms (ISO Standard No.33821:2008).

[9] International Organization for Standardization. Acoustics-measurement of Room acoustics parameters Part 2-Performance Spaces (ISO Standard No.33822:2009).

[10] Vassilantonopoulos, S.; Hatziantoniou, P.; Tatlas, N.A.; Zakynthinos, T.; Skarlatos, D.; Mourtzopoulos, J.N. Measurements and analysis of the acoustics of the ancient theatre of Epidaurus. *The Acoustics of Ancient Theatres Conference 2011*, Patras, Greece, September 18-21, In CD-ROM.